Automatic Resonant Frequency Tracking in Parallel LLC Boost DC–DC Converter

Utsab Kundu, *Student Member, IEEE*, Shiladri Chakraborty, *Student Member, IEEE*, and Parthasarathi Sensarma, *Member, IEEE*

***Abstract*—This paper proposes an automatic resonant frequency tracking scheme for resonant converters. A plant modeling approach is presented based on realistic ramp variation of resonant frequency due to slowly varying environmental conditions. The drift in resonant frequency is detected by observing the phase relationship of an electrical variable pair. A rigorous analysis is carried out to select the most suitable variable pair for phase comparison. The effects of circuit nonidealities on the proposed phase detection technique have been detailed. The proposed control technique has been implemented using low cost analog circuitry and is applied to a parallel *LLC* tank-based resonant boost dc–dc converter. Experimental results are presented on a 160-W prototype to validate the analytical predictions.**

***Index Terms*—DC–DC converter, parallel *LLC* tank, phase comparator, resonant frequency, self-tuning.**

I. Introduction

DEMAND for dc–dc converters for high voltage gain (A_v) is increasingly felt in many recent applications like high intensity discharge (HID) lamps in automobiles (12–120 V)[1], telecom supplies (48–380 V) [2], dc bus supply for grid-side converters in photovoltaic/fuel-cell/battery interfaces [3]–[7] and drive converters in electric/hybrid electric vehicles [8]–[12]. Additional demands on power density require that the source current drawn by these converters be continuous. Classical boost converters are inadequate for these applications since their A_v versus duty-ratio characteristics become concave in continuous conduction mode, given the inevitable presence of parasitic resistances. Cascaded boost converters [13], coupled inductor boost converters [14], and boost converters comprising voltage multiplier cells [15] provide high gain, but have high part count. The *Z*-source inverter [16] has restricted gain and efficiency after incorporating parasitic resistances. Moreover, discontinuity in its A_v characteristic around maximum gain region complicates the control scheme. Some of the aforementioned applications demand galvanic isolation, which allow the designer to achieve any high voltage gain by selecting transformer turns ratio. But transformers having large turns ratio suffer from high leakage inductances, which inevitably increase the voltage stress on switches [17]. A parallel *LLC* resonant boost converter is reported in [18], which successfully provides high A_v along with galvanic isolation, which not only ensures reduction in voltage stress but also achieves soft switching.

In the conventional resonant converters, the switching frequency is used as a control variable to modulate the tank gain [19]–[24]. But if the tank is designed to provide very high gain, the gain characteristic necessarily has an extremely high curvature around the resonant frequency, which makes minute modulation of the switching frequency to achieve precise and steady voltage control practically unrealizable. Hence, to extract maximum gain, the converter is operated [18] at the tank resonant frequency, which, however, drifts due to tank parameter variation leading to reduction in A_v. This reduction could be prevented with an online strategy to tune the converter switching to match the current resonant frequency, which summarizes the motivation and scope of automatic resonant frequency tracking (ARFT) methods.

In the reported literature, frequency tracking has been achieved for parallel resonant converter [25], [26] and *LCC* [27] by sensing the tank input current followed by a phase-locked loop. But this is not applicable for isolated topologies since the tank input current no longer remains in phase with the switching signals, due to the transformer magnetizing current [28]. For isolated converters, a recent ARFT strategy [29] for a series *LLC* tank topology stipulates a two-step approach. First, the switching signals of the secondary side synchronous rectifier (SR) MOSFETs are adjusted to eliminate body diode conduction. Then, a pulsewidth-locked loop (PWLL) is used to equalize the pulsewidth of the primary and SR switches, which in turn ensures the frequency tuning. But this method, which exploits the switching behavior of an antiparallel diode–MOSFET pair, is not applicable for topologies having a diode bridge rectifier in secondary.

This paper presents a different approach for self-tuning, which is based on phase relationship between a pair of unique electrical variables in the resonant tank. Detailed analysis to decide the appropriate variable pair, based on justifiable criteria, is provided. The rest of this paper is organized as follows. Section II reviews the parallel *LLC* tank-based boost topology proposed in [18] and describes the output filter inductor design. Section III details the design of the ARFT controller, while Section IV presents an analytical approach to choose an appropriate variable pair to detect the frequency drift. Section IV analyses the effect of tank nonidealities on the phase relationship of the chosen variable pair. Analog implementation of the proposed control technique is described in Section V. Numerical simulation results are presented

Manuscript received February 10, 2014; revised May 17, 2014; accepted July 21, 2014. Date of publication July 29, 2014; date of current version February 13, 2015. Recommended for publication by Associate Editor C. A. Canesin.

U. Kundu and P. Sensarma are with the Department of Electrical Engineering, Indian Institute of Technology, Kanpur 208016, India (e-mail: utsab@iitk.ac.in; sensarma@iitk.ac.in).

S. Chakraborty is with the Department of Electrical Engineering, Indian Institute of Technology, Kharagpur 721302, India (e-mail: shiladri007@gmail.com).

Digital Object Identifier 10.1109/TPEL.2014.2344021

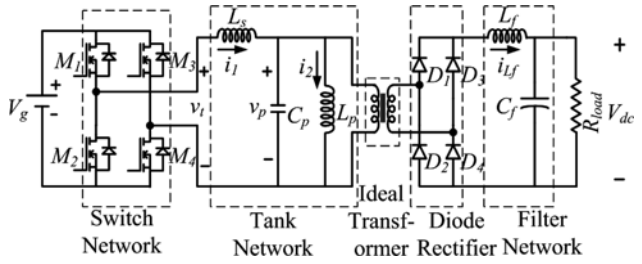

Fig. 1. Parallel *LLC* resonant boost dc–dc converter topology.

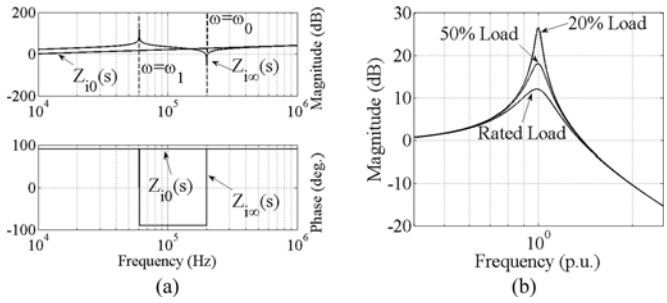

Fig. 2. (a) $Z_{i0}(s)$ and $Z_{i\infty}(s)$. (b) Voltage gain versus p.u. switching frequency.

in Section VI and augmented with experimental results on a 160-W prototype to validate the analysis.

II. Parallel *LLC* Resonant Boost DC–DC Converter Topology

The dc–dc converter topology proposed in [18], depicted in Fig. 1, is basically a high-frequency *LLC* resonant converter. The resonating elements comprise the series inductor L_s transformer magnetizing inductance L_p and the parallel capacitor C_p. The tank is excited through a full-bridge circuit and its output feeds the transformer primary. Rectification of the secondary voltage is done by a diode bridge rectifier followed by a second-order filter for double-frequency attenuation.

A. Properties of the Tank

Fig. 2(a) shows the transfer characteristic of the short-circuit input impedance $Z_{i0}(s)$ and the open-circuit input impedance $Z_{i\infty}(s)$ of the *LLC* tank network given by the following equations [18]:

$$\begin{aligned} Z_{i0}(s) &= sL_s \\ Z_{i\infty}(s) &= sL_s + \left(\frac{1}{sC_p} || sL_p\right) \\ &= s(L_s + L_p) \cdot \frac{1 + s^2/\omega_0^2}{1 + s^2/\omega_1^2} \end{aligned} \tag{1}$$

where

$$\omega_1 = 1/\sqrt{L_p C_p}, \;\; \omega_0 = 1/\sqrt{(L_s \parallel L_p) C_p}. \tag{2}$$

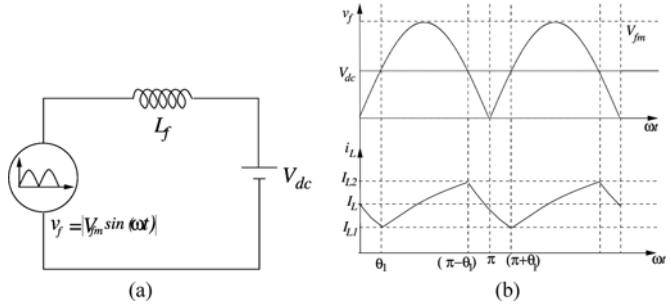

Fig. 3. (a) Diode rectifier circuit. (b) Inductor current waveform.

The tank has two corner frequencies: ω_1, due to L_p and C_p, and ω_0, due to $(L_s \parallel L_p)$ and C_p. From Fig. 2(a), it is clear that for $\omega > \omega_0$, both $Z_{i0}(s)$ and $Z_{i\infty}(s)$ are inductive, which implies inductive loading of the switch network, thus ensuring load independent ZVS [30]. This is an advantage of the voltage stiff *LLC* tank topology compared to the conventional current stiff *LLC* topology [31]–[36]. The maximum voltage gain of the tank at $\omega = \omega_0$ is derived [18] as

$$\left|\frac{V_p(j\omega)}{V_t(j\omega)}\right|_{\omega=\omega_0} = \left[\frac{L_p}{L_s + L_p}\right] R\sqrt{\frac{C_p}{L_s || L_p}}. \tag{3}$$

where R is the equivalent load resistance seen from the transformer primary given by

$$R = \pi^2 R_{\text{load}}/8N^2 \tag{4}$$

where N is the transformer turns ratio. Variations of voltage gain with switching frequency at different load conditions are shown in Fig. 2(b). To achieve peak gain, the converter should always operate at a switching frequency

$$f_s = f_0 = \omega_0/2\pi. \tag{5}$$

B. Filter Inductor Design

While deriving (4), small ripple approximation [30] was applied to the filter inductor current and its validity must be ensured over the entire load range, especially at low-load conditions. Fig. 3(a) shows the diode rectifier output v_f, the filter inductor L_f, and the dc bus voltage V_{dc}. V_{fm} denotes the peak value of v_f. V_{dc} is assumed to be constant and ripple free. The typical waveform of inductor current, i_L, is shown in Fig. 3(b). I_{L2} and I_{L1} are the maximum and minimum values of i_L, respectively, whereas I_L denotes the average value.

From Fig. 3(b), it is obvious that

$$V_{\text{dc}} = 2V_{fm}/\pi = V_{fm}\sin\theta_1 \quad \Rightarrow \quad \sin\theta_1 = 2/\pi. \tag{6}$$

During the interval, $\theta_1 \le \omega t \le \pi$

$$\omega L_f \frac{di_L}{d(\omega t)} = V_{fm}\sin(\omega t) - V_{\text{dc}}. \tag{7}$$

Solving (7) and noting that $i_L = I_{L1}$ at $\omega t = \theta_1$ and $i_L = I_{L2}$ at $\omega t = (\pi - \theta_1)$, the per unit (p.u.) peak to peak inductor current ripple is derived for minimum load condition as

$$(I_{L2} - I_{L1})/I_L = KV_{\text{dc}}^2/\omega L_f P_{0\min} \tag{8}$$

TABLE I
COMPARISON OF INDUCTOR POWER DENSITY WITH OTHER TOPOLOGIES

Topology	L_f (μH)	P_0 (kW)	I_L (A)	$P_0/(L_f I_L^2)$ (W/HA^2)
Parallel *LLC* Boost	10,000	0.160	0.357	125,540
ZVS–ZCS Full Bridge [37]	12	2	41.67	95,984
Natural ZVS Bidirectional [38]	5	1.6	133.3	18,000
Isolated Boost Full Bridge [39]	2.5	3	350	9,796

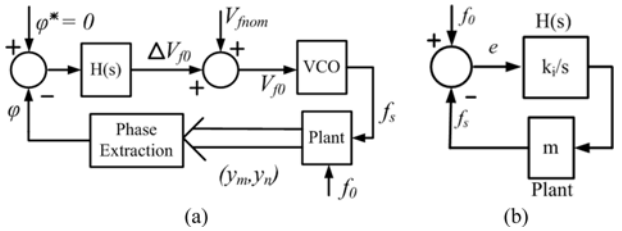

Fig. 4. (a) Proposed Frequency Tracking loop. (b) Simplified block diagram of frequency tracking loop.

where

$$K = \left(\pi\sqrt{1-(4/\pi^2)} + 2\sin^{-1}(2/\pi) - \pi\right). \tag{9}$$

and $P_{0\min}$ is the minimum value of output power (P_0). To restrain this ripple to less than 40% of the average output current at 20% load, the value of L_f has been evaluated from (8) and (9) and is listed in Table I. A direct indication of the inductor power is obtained by comparing $P_0/(L_f I_L^2)$ [30] for some sample topologies [37]–[39], which proves that the filter inductor of the parallel *LLC* boost converter offers the optimal design.

III. PROPOSED ARFT SCHEME

Since the drift in the tank resonant frequency is mainly due to change in ambient conditions, the ARFT scheme is proposed as a slow outer-loop nesting an inner fast voltage control loop. Thus, the bandwidth of this loop is designed at least an order lower than that of the inner loop. With this consideration, the plant, comprising the switch network and tank, is adequately modeled as

$$[i_1\ v_p\ i_2]^T = \underline{\mathbf{G}}_\mathbf{p} v_t,\ \underline{\mathbf{G}}_\mathbf{p} = \left[A_1 e^{j\phi_1}\ A_2 e^{j\phi_2}\ A_3 e^{j\phi_3}\right]^T \tag{10}$$

where A_k and ϕ_k, $k = 1, 2, 3$ are not functions of time but exclusively depend on the tank excitation frequency, f_s. The plant parameters, A_k and ϕ_k, are expressed in terms of *LLC* circuit parameters and have been presented in Appendix B. Assuming realization of a reasonably accurate phase detection network, which, when operating on any two plant variables y_m and y_n, extracts

$$\Delta\phi = \arg\left(y_m \cdot y_n^*\right) \tag{11}$$

a frequency tracking loop is proposed as shown in Fig. 4(a). The proposed control loop is further simplified and depicted in Fig. 4(b). Since the ARFT loop is designed for operation close to the exact resonant frequency, the plant is modeled using a first-order approximation as follows:

$$\Delta\phi = \left(\frac{\partial\phi}{\partial\omega}\bigg|_{\omega_0}\right)\Delta\omega = m\Delta\omega. \tag{12}$$

Controller design is based on ensuring arbitrary steady-state tracking error for a realistic ramp variation in the resonant frequency f_0, given by

$$f_0(t) = F_{0i}(1+\alpha t) \tag{13}$$

where F_{0i} is the initial value of $f_0(t)$ and α the ramp slope. An integral controller $H(s)$ is selected and the integral constant k_i decides the steady-state error $e_{\rm ss}$ as follows:

$$E(s) = F_0(s) - F_s(s) = F_{0i}(s+\alpha)/s(s+mk_i). \tag{14}$$

Using the final value theorem, the steady-state error is

$$e_{\rm ss} = \lim_{s\to 0} sE(s) = (F_{0i}\alpha)/(mk_i). \tag{15}$$

Arbitrary steady-state error $e_{\rm ss}$ is ensured by the integral constant k_i given by

$$k_i = \alpha/me_{\rm sspu},\ \ e_{\rm sspu} = e_{\rm ss}/F_{0i}. \tag{16}$$

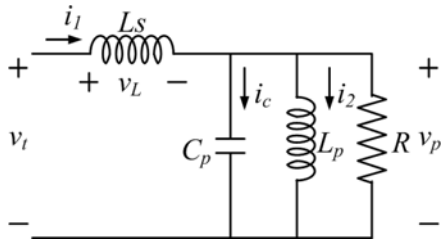

Fig. 5. Parallel *LLC* tank topology.

IV. CHOICE OF A VARIABLE PAIR TO DETECT DETUNING

Fig. 5 shows the circuit diagram of the resonant tank along with the relevant state variables. Denoting the state vector $\mathbf{X} = [i_1\ \ v_p\ \ i_2]^T$ and its time derivative as $\dot{\mathbf{X}} = [v_L\ \ i_C\ \ v_p]^T$, selection of the suitable variable pair begins with the definition of the set $\mathbf{A}$ as well as its Cartesian square $\mathbf{\Pi}$ as follows:

$$\mathbf{A} = \{\mathbf{X}^T, \dot{\mathbf{X}}^T, v_t\} \quad \text{and} \quad \mathbf{\Pi} = \mathbf{A}\times\mathbf{A}. \tag{17}$$

Assuming that the frequency response of the tank network has negligible sidebands, a binary relation Φ is defined on $\mathbf{A}$ as follows:

$$\Phi \subset \Pi \text{ and} \tag{18}$$

$$\Phi\left\{\langle x_m, x_n\rangle : \arg[x_m(j\omega)/x_n(j\omega)] \in (\mathbf{B1}\cup\mathbf{B2})\right\}. \tag{19}$$

The membership of sets $\mathbf{B1}$ and $\mathbf{B2}$ and its implications are explained as follows.

1) $\mathbf{B1}$ is the set with no element a constant. (*Nontriviality*) Trivial 2-tuples are of the form $\langle x, x\rangle$, $\langle x, \dot{x}\rangle$ or $\langle \dot{x}, x\rangle$.

TABLE II
TRANSFER FUNCTIONS OF RELEVANT VARIABLE PAIRS AND THEIR PHASE RELATIONSHIPS

$G_k(s)$	C_{mn}	$N(s)$	$D(s)$	$\tan(\phi)$	$\frac{d\phi}{d\omega_{\rm pu}}\vert_{\omega_{\rm pu}=1}$
$V_p(s)/V_t(s)$	$a/(1+a)$	1	$F_1(s)$	$-\omega_\gamma/\omega_\alpha$	$-2Q_0 = -m_2$
$V_L(s)/V_t(s)$	$1/(1+a)$	$F_2(s)$	$F_1(s)$	$a\omega_\gamma/(\omega_\alpha\omega_\beta+\omega_\gamma^2(1+a))$	$-a\rho(Q_0/\delta) = -m_1$
$V_L(s)/V_p(s)$	$1/a$	$F_2(s)$	1	$\omega_\gamma(1+a)/\omega_\beta$	$(1+a)(2+a)/(Q_0\delta) = m_3$

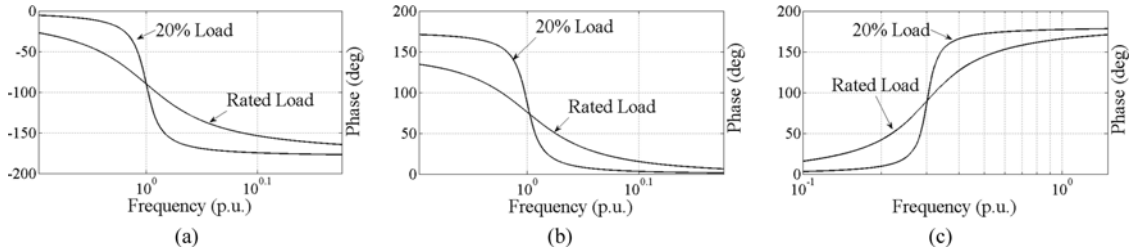

Fig. 6. Phase plots of all feasible variable pairs.

2) **B2** is the set with no two elements, ϕ_m, ϕ_n, satisfying $\phi_m = \pm\phi_n \pm C$(any constant). (*Uniqueness*)
Nonunique pairs of 2-tuples are of these forms: $\langle x_m, x_n\rangle$ and $\langle x_n, x_m\rangle$; $\langle x_m, x_n\rangle$ and $\langle \dot{x}_m, \dot{x}_n\rangle$; $\langle x_m, x_n\rangle$ and $\langle x_m, \dot{x}_n\rangle$; and $\langle x_m, x_n\rangle$ and $\langle x_m, \ddot{x}_n\rangle$.

Using these rules, the final solution set Φ is seen to comprise only three pairs, as indicated in Table II. In case of nonunique pair of 2-tuples, $\langle x_{m1}, x_{n1}\rangle$ and $\langle x_{m2}, x_{n2}\rangle$, which are both nontrivial, preference is given to voltage variables as current measurement would introduce additional impedances in the power circuit.

For each 2-tuple, $\langle x_m, x_n\rangle$ in Φ the corresponding transfer function

$$\frac{x_n(s)}{x_m(s)} \triangleq G_k = C_{mn}\frac{N(s_0)}{D(s_0)}, \qquad s_0 = s/\omega_0 \tag{20}$$

is also listed in Table II, where C_{mn} is a constant, and $N(s_0)$ and $D(s_0)$ are the numerator and denominator polynomials, respectively, in the Laplace operator s normalized by the resonant frequency ω_0. Furthermore, the following definitions were used for concise expression of the quantities listed in Table II:

$$Q_0 = R\sqrt{(1+a)(C_p/L_p)}, \quad a = L_p/L_s \tag{21}$$

$$F_1(s) = s_0^2 + (s_0/Q_0) + 1 \tag{22}$$

$$F_2(s) = s_0^2(1+a) + (s_0/Q_0)(1+a) + 1. \tag{23}$$

It is observed that the modulus of these transfer functions are typically either symmetric or load-dependent around resonant frequency. Hence, the sense of frequency error is not suitably reflected in the gain characteristics. It is for this reason, attention is given to the phase, ϕ (=arg$[G_k(j\omega)]$), as plotted in Fig. 6 at the two extremes of the load range considered. The expressions of $\tan(\phi)$ are listed in the fifth column of Table II, where

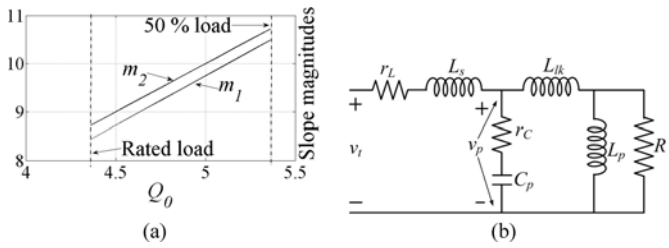

Fig. 7. (a) Variation of phase curve slope magnitudes with Q_0. (b) Nonideal parallel *LLC* tank circuit.

$$\omega_{\rm pu} = \omega/\omega_0, \;\; \omega_\alpha = 1-\omega_{\rm pu}^2 \tag{24}$$

$$\omega_\beta = 1-(1+a)\omega_{\rm pu}^2, \;\; \omega_\gamma = \omega_{\rm pu}/Q_0. \tag{25}$$

In the second step, a localized search for the best candidate transfer function is carried out from the set Π. The chief criterion used is the sensitivity of the phase ϕ to the excitation frequency of the tank input, in the vicinity of the resonance frequency ω_0 and is expressed by modifying (12) as

$$m = \left.\frac{d\phi}{d\omega_{\rm pu}}\right|_{\omega_{\rm pu}=1}. \tag{26}$$

These are listed in Table II using the following definitions:

$$\delta = a^2 + ((1+a)/Q_0)^2, \quad \rho = ((1+a)/Q_0^2) + 2a. \tag{27}$$

Visual inspection of Fig. 6(a)–(c) clearly shows that m_3 is much lower than m_1 or m_2, hence, it is ignored in subsequent investigation. Also evident is that the sensitivity has an inverse relationship with load, hence, its variation is probed in the range 50%–100% of rated load and shown in–Fig. 7(a). Clearly, the pair $\langle v_t, v_p\rangle$ has the greater sensitivity and is, therefore, chosen for ARFT. Substituting $m = m_2 = 2Q_0$ in (16), k_i is selected to limit the steady-state error ($e_{\rm sspu}$) to 0.0004 p.u, for a ramp rate of 0.05 p.u. frequency drift in 20 s, at rated load and the result is tabulated in Table IV.

TABLE III
FREQUENCY DRIFT DUE TO NONIDEALITIES (ALL DATA ARE IN P.U.)

Load condition	$\Delta\omega$	r_L pu	r_C pu	L_{lk} pu
Rated load	0.03	0.1	0.1	0.05
20% load	0.01	0.1	0.1	0.01

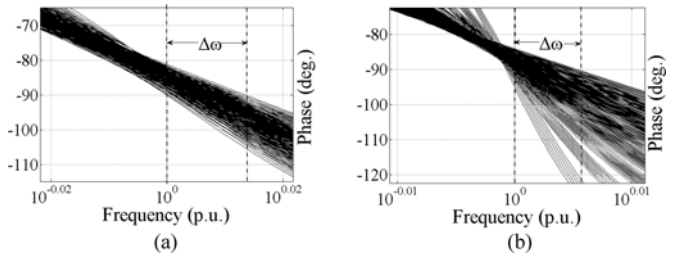

Fig. 8. Phase plots of $V_p(s)/V_t(s)$ considering different combinations of nonidealities.

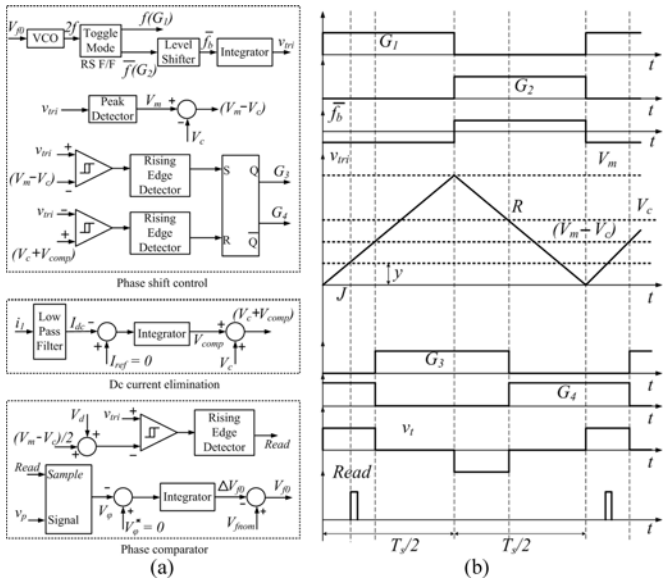

Fig. 9. (a) Control block diagram and (b) ideal waveforms of ARFT.

A. Effects of Tank Nonidealities

Since, so far, the analysis was based on ideal circuit elements, the previous conclusions could arguably be invalidated in practical circuits. To ensure their validity, therefore, the parallel *LLC* tank circuit, shown in Fig. 7(b), is considered with three major nonidealities, viz. transformer leakage inductance, L_{lk}, internal resistance, r_L, and ESR, r_C, of L_s and C_p, respectively. The modified transfer function $V_p(s)/V_t(s)$ is expressed as

$$\frac{V_p(s)}{V_t(s)} = \frac{a_3 s_0^3 + a_2 s_0^2 + a_1 s_0}{b_4 s_0^4 + b_3 s_0^3 + b_2 s_0^2 + b_1 s_0 + 1}. \tag{28}$$

Coefficients of both numerator and denominator polynomials of (28) are detailed in Appendix A. For a realistic variation for $r_{L\mathrm{pu}}$, $r_{C\mathrm{pu}}$ (0–0.1 per unit) and $L_{lk\mathrm{pu}}$ (0–0.05 per unit), two families of phase curves are obtained for the loading extremes with different combinations of $r_{L\mathrm{pu}}$, $r_{C\mathrm{pu}}$, and $L_{lk\mathrm{pu}}$ and shown in Fig. 8. The combinations of nonidealities for which maximum frequency drifts ($\Delta\omega$) take place during rated and 20% load conditions have been listed in Table III. Evidently, for the considered range of nonidealities, it is not possible to detect frequency deviations less than 3% and 1% of the resonant frequency, at maximum and minimum load conditions, respectively.

V. ANALOG REALIZATION OF ARFT

The automatic resonant frequency tracker has been implemented using low-cost analog circuitry. It mainly comprises a phase-shift controller and a phase comparator. However, to restrict the injection of dc current into tank circuit, a dc current elimination scheme has also been incorporated.

A. Phase-Shift Control

The full-bridge circuit is switched using phase-modulated (PM) approach [40]. The block diagram of PM controller is depicted in Fig. 9(a). The voltage-controlled oscillator (VCO) is followed by a flip–flop in toggle mode, which generates complementary switching signals G_1 and G_2, each with 50% duty ratio. The level shifter synthesizes the switching signal G_2 to produce a zero-mean square wave $\bar{f}_b$, which is, subsequently, integrated to produce the carrier triangle v_{tri}. The control voltage V_c decides the overlap angle as switch M_3 is made to turn OFF at the intersection [marked as *R* in Fig. 9(b)] of V_c with v_{tri}. Comparison of v_{tri}, individually with V_c and $(V_m - V_c)$, generates the switching signals G_3 and G_4.

B. DC Current Elimination

Absence of series capacitor in the topology indicates that the tank is not inherently capable of dc rejection. To mitigate this problem, dc component (I_{dc}) of tank input current is extracted using a low-pass filter and integrated as shown in Fig. 9(a). The integrator output (V_{comp}) is added to V_c, which adjusts the turn-off instant of M_3 to eliminate any dc current.

C. Phase Comparator for Self-Tuning

Fig. 6(a) reveals that v_p lags fundamental of v_t by 90° when $f_s = f_0$, at all loads, implying that the positive going zero of v_p coincides with the axis of symmetry of the positive half of v_t [marked as *J* in Fig. 9(b)]. The corresponding voltage level (y) on the carrier triangle, v_{tri} at "*J*" is

$$y = (V_m - V_c)/2. \tag{29}$$

For known V_m and V_c, sampling of v_p is performed precisely at "*J*" in every cycle through comparison of y with v_{tri}, as shown in Fig. 9(a). Since the sampled value, V_ϕ is positive for $f_s < f_0$ and negative for $f_s > f_0$, the sign of frequency error is clearly revealed by V_ϕ. Moreover, as obvious from Fig. 6(a), V_ϕ varies almost linearly for small excursions of f_s around the resonant frequency. Hence, V_ϕ is integrated and the integrator output (ΔV_{f0}) is subtracted from the nominal VCO reference

TABLE IV
SYSTEM SPECIFICATIONS

L_s	L_p	C_p	f_s	N	C_f	V_g	$V_{\rm dc}$	k_i
20 μH	200 μH	33 nF	200 kHz	4	16.5 μF	35 V	400 V	0.6944

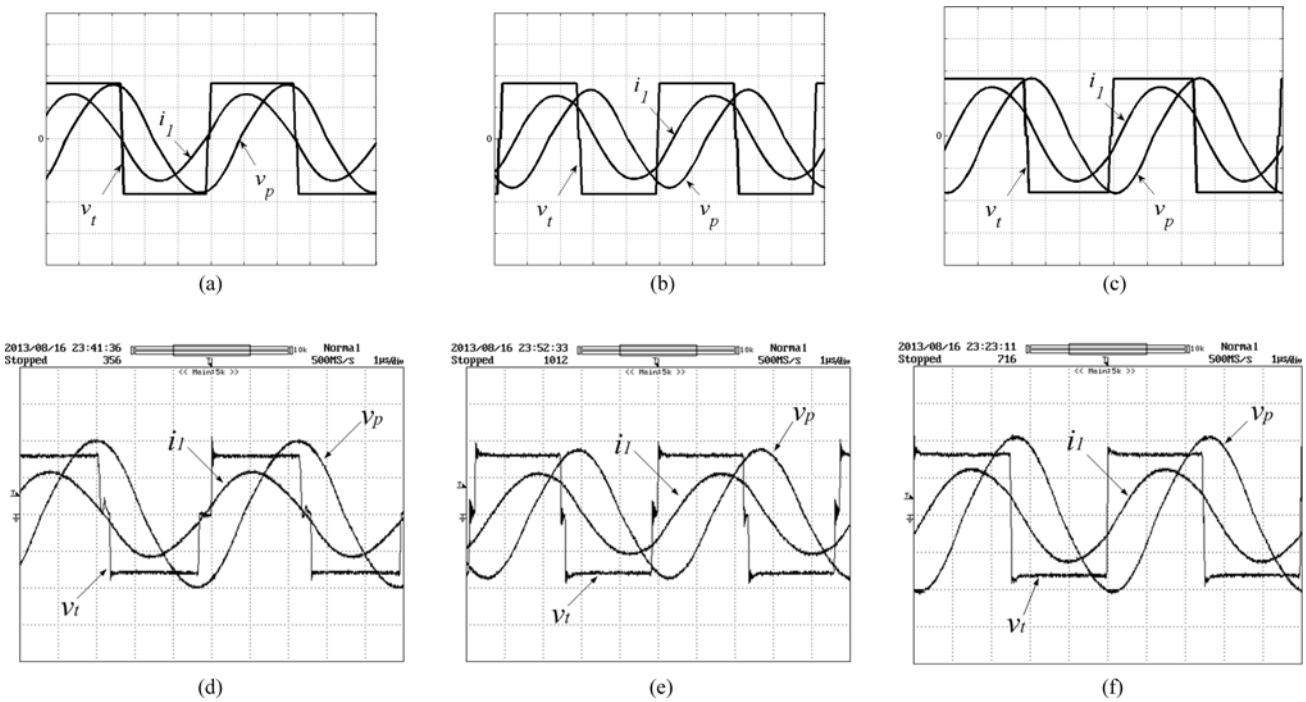

Fig. 10. Performance of frequency tracking controller. Simulation results: (a) open loop ($f_s = 190$ kHz and $f_0 = 200$ kHz), (b) open loop ($f_s = 210$ kHz and $f_0 = 200$ kHz), (c) closed loop ($f_s = f_0 = 200$ kHz). Experimental results: (d) open loop ($f_s = 190$ kHz and $f_0 = 200$ kHz), (e) open loop ($f_s = 210$ kHz and $f_0 = 200$ kHz), (f) closed loop ($f_s = f_0 = 200$ kHz). Scale: v_t (20 V/div), i_1 (5 A/div), v_p (100 V/div); *X*-axis: (Time − 1 μs/div).

$V_{f\rm nom}$. This configuration ensures $V_\phi = V_\phi^* = 0$ in closed loop, and thus, $f_s = f_0$ is ensured. Practical realization of the proposed technique requires a small voltage V_d to be added with $(V_m - V_c)/2$, which is

$$V_d = t_{\rm cor} \times V_m (T_s/2) \tag{30}$$

where

$$t_{\rm cor} = t_{\rm GD} + t_p + t_{d(\rm off)} + t_f) \tag{31}$$

$$-(t_{\rm comp} + t_{\rm RED} + t_{\rm width}). \tag{32}$$

Gate driver delay and propagation delay of dead-time generation circuit are denoted by $t_{\rm GD}$ and t_p, respectively. Delays associated with MOSFETs are turn-off delay $t_{d(\rm off)}$ and fall time t_f. $t_{\rm comp}$ and $t_{\rm RED}$ are propagation delays of comparator and rising edge detector used for phase comparison, respectively. Pulse width of "Read" signal is denoted by $t_{\rm width}$.

VI. RESULTS AND DISCUSSIONS

A model of parallel *LLC* resonant converter and the proposed control scheme is developed in MATLAB Simulink. All system data are listed in Table IV. The experimental prototype to implement the complete analog controller and the power circuit is fabricated on an impedance-controlled circuit board (PCB) using planar magnetics. The performance of the ARFT controller is shown in Figs. 10–13. The resonant frequency f_0 is at 200 kHz and the converter is operating near rated load with zero phase overlap (see Fig. 10). When switching frequency, $f_s = 190$ kHz, i_1 leads v_t and v_p lags v_t by an angle less than 90°. Similarly, when $f_s = 210$ kHz, i_1 lags v_t and v_p lags v_t by an angle greater than 90°. Whereas i_1 lags v_t and v_p lags v_t exactly

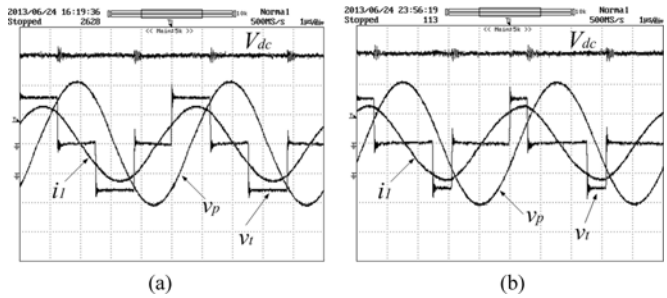

Fig. 11. Closed-loop performance of the frequency tracking controller under different load conditions. Experimental results: (a) 50% load, (b) 20% load. Scale: v_t (20 V/div), i_1 (5 A/div), v_p (100 V/div), $V_{\rm dc}$ (100 V/div); *X*-axis: (Time − 1 μs/div).

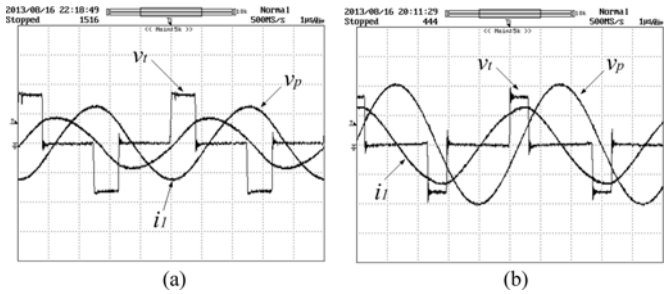

Fig. 12. Performance of the frequency tracking controller. Experimental results: (a) open loop ($f_s = 200$ kHz and $f_0 = 185$ kHz), (b) closed loop ($f_s = f_0 = 185$ kHz). Scale: v_t (20 V/div), i_1 (5 A/div), v_p (100 V/div); *X*-axis: (Time − 1 μs/div).

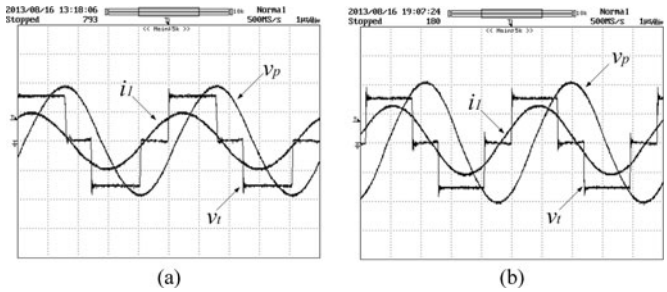

Fig. 13. Performance of the frequency tracking controller. Experimental results: (a) open loop ($f_s = 200$ kHz and $f_0 = 208$ kHz), (b) closed loop ($f_s = f_0 = 208$ kHz). Scale: v_t (20 V/div), i_1 (5 A/div), v_p (100 V/div); *X*-axis: (Time − 1 μs/div).

by 90° during closed-loop operation, which supports the analysis of the previous section. Closed-loop performance of the ARFT controller under different load conditions is depicted in Fig. 11, which also shows the output dc bus voltage $V_{\rm dc}$. Now, the resonant frequency is changed to 185 kHz by increasing the value of the capacitor C_p and the converter is operated at 30-W load with an overlap angle of 150°. Open-loop and closed-loop results are shown in Fig. 12. Similarly, open-loop and closed-loop results for resonant frequency 208 kHz is shown in Fig. 13 when the converter operates at 80-W load with an overlap angle of 75°. To verify the tracking performance of the ARFT controller, a variable inductor is emulated. A component of the series inductor L_s is varied almost linearly so that the net series inductance is expressed as

$$L_s(t) = L_{si}(1 + \beta t) \tag{33}$$

where L_{si} is the initial value of L_s and β the ramp slope. The resonant frequency variation under this condition is derived from (2), (5), and (33) assuming $(L_{si} + L_p) \gg L_{si}\beta t$ and expressed as

$$f_0(t) = F_{0i}(1 - \beta t/2) \tag{34}$$

where

$$F_{0i} = 1/2\pi\sqrt{L_{si}L_pC_p/(L_{si} + L_p)}. \tag{35}$$

Defining

$$\Delta f_0(t) = f_{\rm nom} - f_0(t), \quad \Delta F_{0i} = f_{\rm nom} - F_{0i} \tag{36}$$

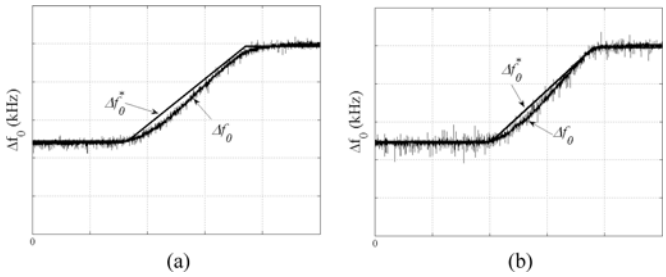

Fig. 14. Performance of the frequency tracking controller under ramp variation in resonant frequency. Experimental results: (a) rated load, (b) 20% load. Scale: Δf_0 (3.58 kHz/div); *X*-axis: (Time − 10 s/div).

TABLE V
P.U. STEADY-STATE FREQUENCY ERROR

Load condition	L_{sf} (μH)	L_{si} (μH)	t_r (s)	$e_{\rm sspu}$ (analytical)	$e_{\rm sspu}$ (experimental)
Rated	25	22.7	20.5	4.1×10^{-4}	5×10^{-4}
20% load	25	22.7	17.8	8.8×10^{-5}	9.3×10^{-5}

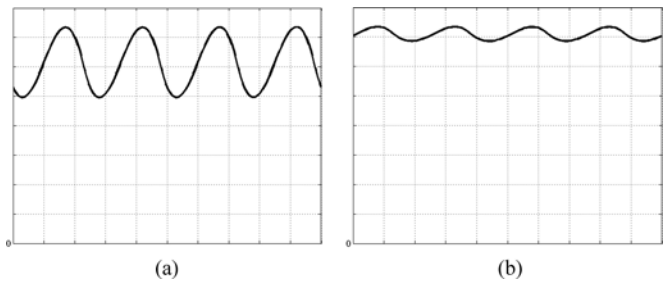

Fig. 15. Filter inductor current (a) at 20% load (0.01 A/div), (b) at rated load (0.05 A/div); *X*-axis: (Time − 1 μs/div).

where $f_{\rm nom}$ is the predefined base value of the resonant frequency. Equation (34) is rearranged as

$$\Delta f_0(t) = \Delta F_{0i} + \beta F_{0i}t/2. \tag{37}$$

Following the same steps as in (14) and (15), the p.u. steady-state frequency error, $e_{\rm sspu}$, is derived as

$$e_{\rm sspu} = \beta/(2m_2k_i). \tag{38}$$

The tracking performance of the ARFT controller is shown in Fig. 14 for two extreme load conditions, where Δf_0^* denotes the reference. Analytical and experimental values of $e_{\rm sspu}$ is given in Table V, where L_{sf} denotes the final value of L_s and t_r is the duration of ramp. Close agreement of these results validates the controller design.

The filter inductor currents at rated load (160 W) and at 20% load conditions are shown in Fig. 15. At low load, peak-to-peak filter inductor current ripple is 35% of the average current, which is sufficiently low to validate the approximation of ac resistance across the tank capacitor. Fig. 16 depicts the tank input current with and without the dc elimination loop. It is clear that this loop ensures zero-mean tank input current and removes any chance of the transformer saturation.

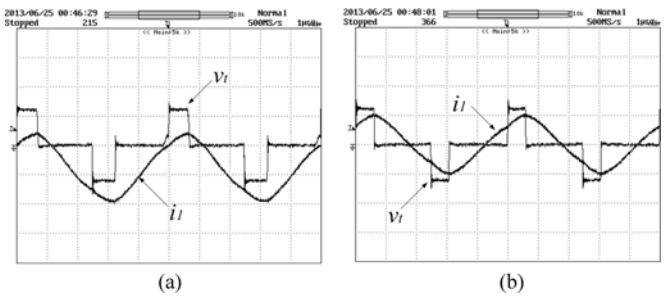

Fig. 16. Performance of dc current elimination loop. Experimental results: (a) open loop, (b) closed loop. Scale: v_t (20 V/div), i_1 (2 A/div); *X*-axis: (Time − 1 μs/div).

VII. Conclusion

This paper presents the detailed analysis, design, and realization of a self-tuning method for resonant converters, with specific consideration of a three-element, parallel *LLC* circuit. The governing equations of the converter are presented along with its voltage gain and associated resonance/antiresonance modes. A closed-loop ARFT algorithm is proposed to ensure self-tuning under parameter variations due to environmental conditions. The relevant plant model is derived and necessity of an accurate phase detector is noted. Selection of the most suitable input variable pair for the phase detector is carried out through rigorous analysis and the achievable resolution of the phase detector is derived for a realistic range of circuit nonidealities. It is emphasized that this analysis is presented in a general form and applicable for any other resonant converter topology. Analog circuit realization of the phase detector is presented in appropriate detail. Analytical predictions regarding the performance of the ARFT scheme are experimentally validated by drifting the tank resonant frequency from its initial designed value. This paper, thus, establishes a tractable approach toward solving the perennial problem of resonance drift in resonant converters.

Appendix A
Coefficients of $V_p(s)/V_t(s)$

$$
\begin{aligned}
a_3 &= a\omega_0 r_{C\mathrm{pu}} L_{lk\mathrm{pu}} \\
a_2 &= a(\omega_0 L_{lk\mathrm{pu}} + \eta r_{C\mathrm{pu}} Q_0 \omega_\zeta) \\
a_1 &= \eta Q_0 \omega_\zeta \\
b_4 &= \omega_0^3 L_p C_p L_{lk\mathrm{pu}} \\
b_3 &= \omega_0(\omega_0^2 L_p C_p L_{lk\mathrm{pu}} r_{L\mathrm{pu}} \\
&\quad + aL_{lk\mathrm{pu}} r_{C\mathrm{pu}} + r_{C\mathrm{pu}} + \omega_0 \eta Q_0/\omega_\sigma) \\
b_2 &= \omega_0(1 + r_{C\mathrm{pu}} r_{L\mathrm{pu}} + aL_{lk\mathrm{pu}}) + \omega_0^2 \eta Q_0 r_{L\mathrm{pu}}/\omega_\sigma \\
&\quad + Q_0 r_{C\mathrm{pu}} \omega_\zeta (1 + a\eta) \\
b_1 &= \omega_0 r_{L\mathrm{pu}} + Q_0 \omega_\zeta (1 + r_{C\mathrm{pu}} r_{L\mathrm{pu}} + a\eta) \\
b_0 &= r_{L\mathrm{pu}} Q_0 \omega_\zeta .
\end{aligned}
$$

where

$$
\begin{aligned}
L_{lk\mathrm{pu}} &= L_{lk}/L_p, \;\; r_{L\mathrm{pu}} = r_L/(\omega_0 L_s), \;\; r_{C\mathrm{pu}} = \omega_0 C_p r_C \\
\eta &= 1 + L_{lk\mathrm{pu}}, \;\; \omega_\sigma = \sqrt{(1+a)/L_p C_p} \\
\omega_\zeta &= 1/\sqrt{(1+a)L_p C_p}.
\end{aligned}
$$

Appendix B
Plant Parameters

TABLE VI

k	A_k	$\tan(\phi_k)$
1	$\sqrt{aL_s C_p(\psi_2^2 + \psi_3^2)}/(\omega_{\mathrm{pu}} \psi_1 \sqrt{1+a})$	$-\psi_3/\psi_2$
2	$a/(\sqrt{\psi_1}(a+1))$	$-\omega_\gamma/\omega_\alpha$
3	$\sqrt{aC_p}/(\omega_{\mathrm{pu}}(1+a)\sqrt{L_s(1+a)\psi_1})$	$\omega_\alpha/\omega_\gamma$

where

$$
\begin{aligned}
\psi_1 &= \omega_\gamma^2 + \omega_\alpha^2 \\
\psi_2 &= (\omega_{\mathrm{pu}} \omega_\alpha (1+a)/Q_0) - \omega_\beta \omega_\gamma \qquad (39) \\
\psi_3 &= \omega_\alpha \omega_\beta + (\omega_{\mathrm{pu}} \omega_\gamma (1+a)/Q_0). \qquad (40)
\end{aligned}
$$

Acknowledgment

The authors would like to acknowledge Mr. A. K. Basu and Mr. Nandkishore for their support during development of the experimental hardware.

References

[1] O. Abutbul, A. Gherlitz, Y. Berkovich, and A. Ioinovici, "Step-up switching-mode converter with high voltage gain using a switched-capacitor circuit," *IEEE Trans. Circuits Syst. I*, vol. 50, no. 8, pp. 1098–1102, Aug. 2003.

[2] J. Akerlund, "48 V DC computer equipment topology-an emerging technology," in *Proc. IEEE 20th Int. Telecommun. Conf.*, 1998, pp. 15–21.

[3] A. Timbus, M. Liserre, R. Teodorescu, P. Rodriguez, and F. Blaabjerg, "Evaluation of current controllers for distributed power generation systems," *IEEE Trans. Power Electron.*, vol. 24, no. 3, pp. 654–664, Mar. 2009.

[4] C.-L. Chen, Y. Wang, J.-S. Lai, Y.-S. Lee, and D. Martin, "Design of parallel inverters for smooth mode transfer microgrid applications," *IEEE Trans. Power Electron.*, vol. 25, no. 1, pp. 6–15, Jan. 2010.

[5] Y. W. Li and C.-N. Kao, "An accurate power control strategy for power-electronics-interfaced distributed generation units operating in a low-voltage multibus microgrid," *IEEE Trans. Power Electron.*, vol. 24, no. 12, pp. 2977–2988, Dec. 2009.

[6] Y.-M. Chen, A. Q. Huang, and X. Yu, "A high step-up three-port DC–DC converter for stand-alone PV/battery power systems," *IEEE Trans. Power Electron.*, vol. 28, no. 11, pp. 5049–5062, Nov. 2013.

[7] F. Nejabatkhah, S. Danyali, S. H. Hosseini, M. Sabahi, and S. M. Niapour, "Modeling and control of a new three-input DC–DC boost converter for hybrid PV/FC/battery power system," *IEEE Trans. Power Electron.*, vol. 27, no. 5, pp. 2309–2324, May 2012.

[8] S. Dwari and L. Parsa, "A novel high efficiency high power interleaved coupled-inductor boost DC–DC converter for hybrid and fuel cell electric vehicle," in *Proc. IEEE Vehicle Power Propulsion Conf.*, Sep. 9–12, 2007, pp. 399–404.

[9] W. Qian, H. Cha; F.-Z. Peng, and L. M. Tolbert, "55-kW variable 3X DC-DC converter for plug-in hybrid electric vehicles," *IEEE Trans. Power Electron.*, vol. 27, no. 4, pp. 1668–1678, Apr. 2012.

[10] O. Hegazy, R. Barrero, J. Van Mierlo, P. Lataire, N. Omar, and T. Coosemans, "An advanced power electronics interface for electric vehicles applications," *IEEE Trans. Power Electron.*, vol. 28, no. 12, pp. 5508–5521, Dec. 2013.
[11] H. Van Hoek, M. Neubert, R. W. De Doncker, "Enhanced modulation strategy for a three-phase dual active bridge boosting efficiency of an electric vehicle converter," *IEEE Trans. Power Electron.*, vol. 28, no. 12, pp. 5499–5507, Dec. 2013.
[12] O. Hegazy, J. Van Mierlo, and P. Lataire, "Analysis, modeling, and implementation of a multidevice interleaved DC/DC converter for fuel cell hybrid electric vehicles," *IEEE Trans. Power Electron.*, vol. 27, no. 11, pp. 4445–4458, Nov. 2012.
[13] F. L. Luo and H. Ye, "Positive output cascade boost converters," *Proc. IEE*, vol. 151, no. 5, pp. 590–606, Sep. 2004.
[14] T.-F. Wu, Y.-S. Lai, J.-C. Hung, and Y.-M. Chen, "Boost converter with coupled inductors and buck boost type of active clamp," *IEEE Trans. Ind. Electron.*, vol. 55, no. 1, pp. 154–162, Jan. 2008.
[15] M. Prudente, L. L. Pfitscher, G. Emmendoerfer, E. F. Romaneli, and R. Gules, "Voltage multiplier cells applied to non-isolated DC-DC converters," *IEEE Trans. Power Electron.*, vol. 23, no. 2, pp. 871–887, Mar. 2008.
[16] F. Z. Peng, "Z source inverter," *IEEE Trans. Ind. Appl.*, vol. 39, no. 2, pp. 504–510, Mar. 2003.
[17] S. D. Johnson, A. F. Witulski, and R. W. Erickson, "Comparison of resonant topologies in high-voltage DC applications," *IEEE Trans. Aerosp. Electron. Syst.*, vol. 23, no. 3, pp. 263–274, May 1988.
[18] S. Chakraborty and P. Sensarma, "High gain high efficiency front end resonant DC-DC boost converter for PV microinverter," in *Proc. IEEE Energy Convers. Congr. Expo.*, Sep. 15–20, 2012, pp. 180–187.
[19] R. L. Steigerwald, "A comparison of half-bridge resonant converter topologies," *IEEE Trans. Power Electron.*, vol. 3, no. 2, pp. 174–182, Apr. 1988.
[20] K. Al Haddad, A. Bellahnid, V. Rajagopalan, Y. Cheron, and H. Foch, "Novel control strategy to improve the dynamic performance of series resonant converters," in *Proc. IEEE Ind. Appl. Soc. Annu. Meet.*, 1988, pp. 806–812.
[21] R. Liu, C. Q. Lee, "The LLC-type series resonant converter-variable switching frequency control," in *Proc. IEEE 32nd Midwest Symp. Circuits Syst.*, 1989, pp. 509–512.
[22] A. C. Lippincott, R. M. Nelms, M. Garbi, and E. Strickland, "A series resonant converter with constant on-time control for capacitor charging applications," in *Proc. IEEE Appl. Power Electron. Conf.*, Mar. 1990, pp. 147–154.
[23] A. C. Lippincott and R. M. Nelms, "A capacitor-charging power supply using a series-resonant topology, constant on-time/variable frequency control, and zero-current switching," *IEEE Trans. Ind. Electron.*, vol. 38, no. 6, pp. 438–447, Dec. 1991.
[24] R. Liu, C. Q. Lee, and A. K. Upadhyay, "Experimental study of the LLC type series resonant converter," in *Proc. IEEE Appl. Power Electron. Conf.*, 1991, pp. 31–37.
[25] T. J. Ribarich and J. J. Ribarich, "A new procedure for high-frequency electronic ballast design," *IEEE Trans. Ind. Appl.*, vol. 37, no. 1, pp. 262–267, Jan./Feb. 2001.
[26] H. Sheng, Y. Pei, X. Yang, F. Wang, C. W. Tipton, "Frequency tracking control for cap-charging parallel resonant converter with phase-locked loop," in *Proc. IEEE Appl. Power Electron. Conf.*, 2007, pp. 1287–1292.
[27] Y. Yin, M. Shirazi, and R. Zane, "Electronic ballast control IC with digital phase control and lamp current regulation," *IEEE Trans. Power Electron.*, vol. 23, no. 1, pp. 11–18, Jan. 2008.
[28] F. Weiyi, P. Mattavelli, F. C. Lee, and F. Dianbo, "LLC converters with automatic resonant frequency tracking based on synchronous rectifier (SR) gate driving signals," in *Proc. IEEE Appl. Power Electron. Conf.*, Mar. 6–11, 2011, pp. 1–5.
[29] W. Feng, P. Mattavelli, and F. C. Lee, "Pulsewidth locked loop (PWLL) for automatic resonant frequency tracking in LLC DCDC transformer (LLC-DCX)," *IEEE Trans. Power Electron.*, vol. 28, no. 4, pp. 1862–1869, Apr. 2013.
[30] R. W. Erickson, and D. Maksimovic, "Fundamentals of Power Electronics," 2nd ed. New York, NY, USA: Springer, 2000.
[31] B. Yang, F. C. Lee, A. J. Zhang, and G. Huang, "LLC resonant converter for front end DC/DC conversion," in *Proc. IEEE Appl. Power Electron. Conf.*, 2002, pp. 1108–1112.
[32] L. Bing, L. Wenduo, L. Yan , F. C. Lee, J. D. Van Wyk, "Optimal design methodology for LLC resonant converter," in *Proc. IEEE Appl. Power Electron. Conf.*, Mar. 2006, pp. 533–538.
[33] P. Vinciarelli, "Factorized power architecture with point of load sine amplitude converters," U.S. Patent 6984965B2, Jan. 10, 2006.
[34] F. Xiang, H. Haibing, Z. J. Shen, and I. Batarseh, "Operation mode analysis and peak gain approximation of the LLC resonant converter," *IEEE Trans. Power Electron.*, vol. 27, no. 4, pp. 1985–1995, Apr. 2012.
[35] Q. Zhang, C. Hu, L. Chen, A. Amirahmadi, N. Kutkut, Z. J. Shen, and I. Batarseh, "A center point iteration MPPT method with application on the frequency-modulated LLC microinverter," *IEEE Trans. Power Electron.*, vol. 29, no. 3, pp. 1262–1274, Mar. 2014.
[36] K.-B. Park, B.-H. Lee, G.-W. Moon, and M.-J. Youn, "Analysis on center-tap rectifier voltage oscillation of LLC resonant converter," *IEEE Trans. Power Electron.*, vol. 27, no. 6, pp. 2684–2689, Jun. 2012.
[37] J. G. Cho, J. A. Sabate, G. Hua, and F. C. Lee, "Zero-voltage and zero-current-switching full bridge PWM converter for high power applications," in *Proc. IEEE Power Electron. Spec. Conf.*, Jun. 20–25, 1994, pp. 102–108.
[38] L. Hui, F. Z. Peng, and J. S. Lawler, "A natural ZVS high-power bi-directional DC-DC converter with minimum number of devices," in *Proc. IEEE Ind. Appl. Conf.*, Sep. 30–Oct. 4, 2001, pp. 1874–1881.
[39] L. Zhu, "A novel soft-commutating isolated boost full-bridge ZVS-PWM DC-DC converter for bidirectional high power applications," in *Proc. IEEE Power Electron. Spec. Conf.*, Jun. 20–25, 2004, pp. 2141–2146.
[40] J. G. Hayes and M. G. Egan, "A comparative study of phase-shift, frequency, and hybrid control of the series resonant converter supplying the electric vehicle inductive charging interface," in *Proc. IEEE Appl. Power Electron. Conf.*, Mar. 14–18, 1999, pp. 450–457.

Utsab Kundu (S'14) received the B.E. degree in electrical engineering from the Indian Institute of Engineering Science and Technology (formerly Bengal Engineering and Science University), Howrah, India, in 2010 and the M.E. degree in machine drives and power electronics from Indian Institute of Technology (IIT) Kharagpur, Kharagpur, India, in 2012. In 2010, he joined IIT Kharagpur for post-graduate course and carried out research projects on notebook adapter and telecom power supply. He is currently working toward the Ph.D. degree in the Department of Electrical Engineering, IIT Kanpur, Kanpur, India.

His research interests include power converter topologies, modeling, and control techniques.

Shiladri Chakraborty (S'14) received the B.E. degree from Jadavpur University, Kolkata, India, in 2008 and the M.Tech. degree from the Indian Institute of Technology, Kanpur, India, in 2012, both in electrical engineering. He is currently working toward the Ph.D. degree in the Electrical Engineering Department, Indian Institute of Technology, Kharagpur, India.

From 2008 to 2010, he worked as an Assistant Manager at Tata Motors Limited. His research interests include PV inverters, dual-active bridge converters, resonant converters, and modeling of converter magnetics.

Parthasarathi Sensarma (M'00) received the B.E.E. degree from Jadavpur University, Kolkata, India, in 1990, the M.Tech. degree from the Indian Institute of Technology, Kharagpur, India, in 1992, and the Ph.D. degree from the Indian Institute of Science, Bangalore, India, in 2001, all in electrical engineering.

He had held positions in Bharat Bijlee Ltd., Thane, India, CESC Ltd., India, and ABB Corporate Research, Baden-Daettwil, Switzerland, where he was a Staff Scientist with the Power Electronics Department. Since 2002, he has been with the Department of Electrical Engineering, IIT Kanpur, where he is currently a Professor, teaching courses on Power Electronics and Electrical Engineering. His research interests include power quality, FACTS devices, power converters, and renewable energy integration.